Engineering Structures 323 (2025) 119215

Contents lists available at ScienceDirect

Engineering Structures

journal homepage: www.elsevier.com/locate/engstruct

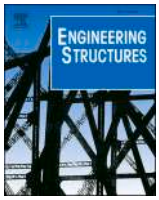

Intrados FRCM-strengthening of a masonry bridge: Experimental and analytical investigations

Paolo Zampieri [a,b,*], Riccardo Piazzon [a], Davide Santinon [a], Lorenzo Hofer [a], Klajdi Toska [a], Flora Faleschini [a], Carlo Pellegrino [a], Franco Iacobini [c], Andrea Vecchi [c], Francesco Iodice [c], Domenico Ricci [c]

[a] Department of Civil, Environmental and Architectural Engineering, University of Padua, Italy
[b] Department of Industrial Engineering, University of Padua, Italy
[c] Rete Ferroviaria Italiana (RFI), Piazza della Croce Rossa 1, Roma 00161, Italy

ARTICLE INFO

Keywords:
Masonry bridges
FRCM composites
Masonry
Limit analysis
Strengthening systems

ABSTRACT

This paper will present the results of an experimental campaign aimed to study the structural behavior of solid clay brick masonry arch models strengthened at the intrados with Fiber Reinforced Cementitious Matrix (FRCM). The arch models' peculiarities are: i) the presence of the haunching made of hydraulic lime mortar-based conglomerate, and ii) the geometry that reproduces a 1:2 scaled longitudinal section of a typical Italian railway single span bridge. The arch models are tested, imposing loading-unloading cycles to analyze the effectiveness of the strengthening system. The results are expressed in terms of failure mode, load carrying capacity and ductility, which shows the increase in the strength and displacement capacity of the strengthened model. Finally, limit analysis was performed to validate the experimental results and to assess the maximum fiber strain and the corresponding stress at the peak load.

1. Introduction

In some cases, the load-bearing capacity of railway masonry bridges in service is not sufficient to withstand the current traffic loads [1–10], seismic action and the other external loads defined by current Standards not considered in the design process.

Since these constructions were built more than 100 years ago, the material is subject to degradation due to weathering, and the structure suffers damage due to traffic loads or other actions (foundation settlements, seismic events, etc) [11–14].

Considering the architectural and strategical value of these structures, the necessity to reestablish adequate safety performance arises. If the restoration to the original structural condition is not sufficient to achieve this objective, the masonry arch should be subjected to retrofitting interventions.

Strengthening systems aim to increase the load-bearing capacity of the arch to vertical and horizontal loads [15]. Traditional strengthening techniques involve inserting of transverse prestressed cables, metal or wooden centering applied to the arch intrados, reinforced and unreinforced concrete cover at the extrados or intrados of the arch, applying tie-rods [16–19]. These techniques can be effective, but they have the drawbacks of being aesthetically obtrusive or adding a significant increase in weight and stiffness to the structure. Less obtrusive and higher-performance technologies, such as FRP and FRCM, have been introduced in the last three decades. These composite systems consist of a matrix that allows a bond within the substrate and the fiber that is embedded in it. This solution permits the introduction of a tensile resistant element that allows the thrust line to exit the arch shape, allowing an increase in arch strength without significantly changing mass and stiffness [20,21]. Among the several types of fibers utilized, experimental campaigns have been conducted on carbon fibers, basalt fibers, glass fibers, PBO, steel wires and natural fibers. The matrix used can be either polymer-based (FRP) or cementitious-based (FRCM); these two systems differ in their compatibility with the support and application methodologies [22–28].

To highlight the contribution of the composite system at the local level, few experimental campaigns have been conducted that apply distinct types of FRCM to masonry supports, considering arch curvatures, highlighting failure modes and system effectiveness [29–36]. The necessity of studying the behavior of masonry arch bridges under

* Corresponding author at: Department of Civil, Environmental and Architectural Engineering, University of Padua, Italy.
E-mail address: paolo.zampieri@unipd.it (P. Zampieri).

https://doi.org/10.1016/j.engstruct.2024.119215
Received 16 July 2024; Received in revised form 3 October 2024; Accepted 21 October 2024
Available online 7 November 2024

controlled laboratory conditions allows for a better understanding of failure mechanisms, an assessment of the influence of all structural elements, and the provision of empirical data to the academic community [37,38]. These results can be compared with numerical models to facilitate their calibration. Experimental laboratory tests were conducted on strengthened arches and vaults to simulate the application of such a system in practical use. Different geometries and types of strengthening system have been tested, showing an increase in bearing capacity and displacement capacity respect the unstrengthened configuration [39–51]. In literature, it is possible to find case studies of FRCM applications to historic buildings, highlighting application methods and results [51–53]. To predict the contribution of the strengthened structures, numerical and analytical methods have been developed, providing static assessment before the composite system is applied in situ. The main analytical method to assess the capacity of the masonry arch is the limit analysis that permits to obtain a bearing load value once the collapse mechanism is defined [54–59]. Through numerical techniques, such as FEM and DEM, it is possible to calibrate the model based on experimental results and simulate the behavior of the tensile and bond properties of the strengthening system and the structural behavior of the whole masonry arch [60–67].

This paper presents the results obtained from an experimental campaign aimed at investigating the behavior of masonry bridges strengthened by means of an FRCM system applied to the arch intrados. The vault geometry was selected to simulate, at a 1:2 scale, a 6-meter span masonry bridge strengthened with a single layer of FRCM. The literature contains numerous studies that examine the effect of strengthening system on stand-alone masonry arches. In this work, in addition to scaling the typical dimensions of arches used in masonry bridges, the effect of haunching made of hydraulic lime-based conglomerate was considered. In the context of understanding the contribution of each element, this study aims to provide insight into the phenomenon; however, it represents an intermediate step toward a comprehensive analysis. Future studies will be necessary to account for the presence of the infill and all structural components not considered in the current experiment. The results are presented as load-displacement curves, a discussion of the collapse mechanism and a comparison between the strengthened and unstrengthened case, highlighting the contribution of fiber in global and local mechanical behaviors. An analytical evaluation considering the finite strength of the masonry and the constitutive law of strengthening system in a simplified approach is illustrated, with the aim of validating the experimental results and offering a tool for simplified evaluation of the contribution of the strengthening system.

2. Experimental program

2.1. Specimens' description

The experimental program was conducted to investigate the structural behavior of intrados FRCM - strengthened masonry bridges. For this purpose, two solid brick arch models with a span of 299 cm, an arch rise of 132.21 cm, an arch thickness of 25 cm and a depth of 51 cm were built in accordance with traditional procedures by experienced masons (see Fig. 1) to reproduce in 1:2 scale a single-span railway arch bridge. The haunching of Italian railway masonry bridges, as evidenced by extensive experimental campaigns (conducted by some of the authors), in many cases consists of a stiffned conglomerate. That is why the haunching in the arch models was realised with a mortar-based conglomerate made of the hydraulic mortar used for the arch joints and aggregates with a maximum diameter of 16 mm. The arch instead was made of solid fired-clay bricks (25 ×12 x 5.5 cm^3) and natural hydraulic lime mortar (with maximum aggregate diameter less than 2 mm) and it was composed of 67 staggered courses, where the radial joints had a thickness of 10 mm at the intrados and about 21 mm at the extrados.

The two arches were built on two rigid reinforced concrete footings

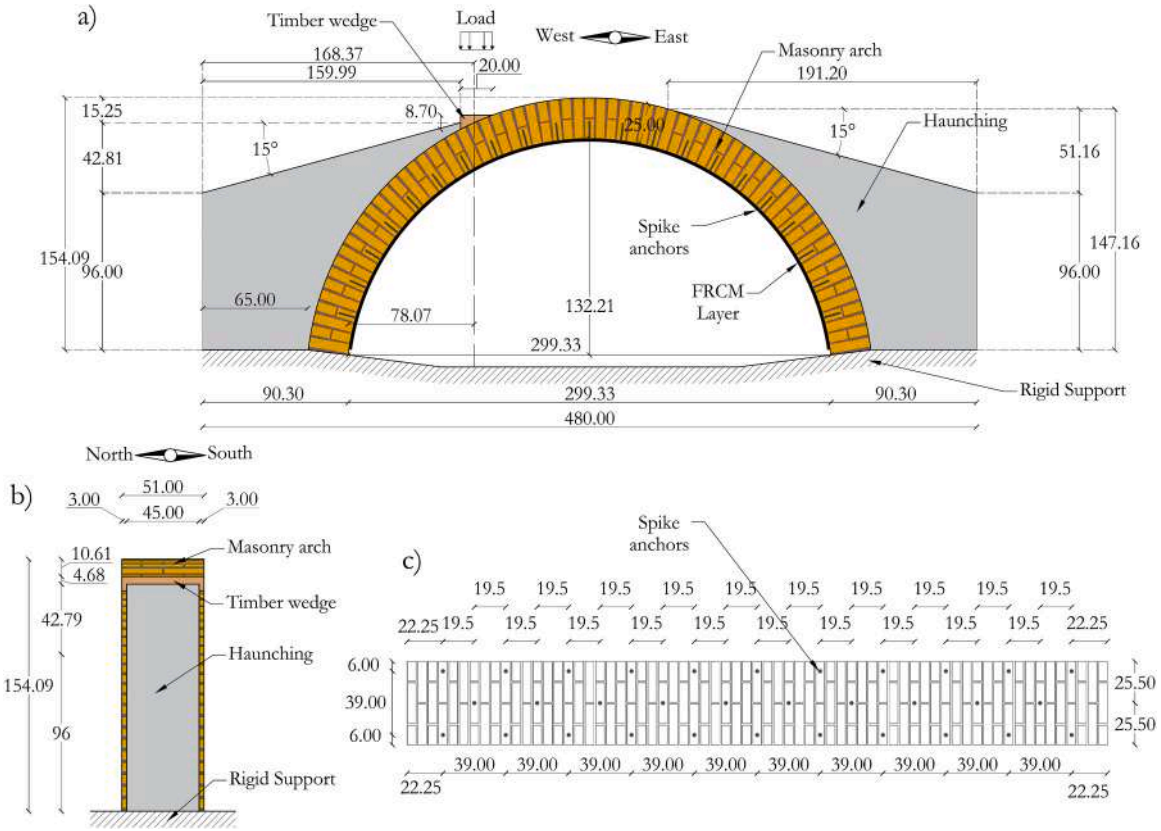

Fig. 1. Geometry of the masonry arch, a) front and b) side c) stretched intrados.

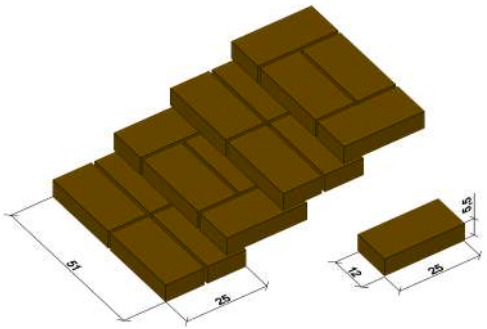

Fig. 2. Masonry arch texture.

supported by ribs. After 28 days of maturation (in wetted condition of the masonry), the haunchings were cast and, after an additional 28 days, the unstrengthened arch model (UM) was tested while the other arch model (SM) was strengthed with a 1 centimiter layer of FRCM applied onto arch intrados and then tested after the FRCM maturation (28 days). The FRCM strengthening system used consisted of one layer of a carbon bidirectional fabric (in dry form) and two 5 mm thick layers of a cementitious matrix. The textile had longitudinal and transversal bundles spaced at 17 mm on center as it is detailed in Zampieri et al., 2023 [36]. The same type of spike anchors used in the experimental campaign presented in Zampieri et al., 2023 [36] were inserted in the arch intrados following the scheme reported in Fig. 1c to increase the connection between masonry and strengthening system.

The strengthening system was applied onto the arch intrados considering the following steps:

- Masonry surface preparation and water saturation of the surface prior to FRCM application,
- Drilling the arch intrados (Fig. 1c),
- Dust removal inside the holes and application of the spike anchors by means of epoxy resin (Fig. 3a),
- Application of the first layer of the mortar,
- Application of the FRCM reinforcement (Fig. 3(b)), shaped as a single strip with dimension equal of the arch intrados surface.
- -the anchors were fanned out (by means of epoxy resin) and then the second layer of mortar was applied (Fig. 3c).

2.2. Materials characterization

The compressive tests are performed on the bricks (UNI EN 772–1:2015), obtaining an average value of 42.51 MPa (st.dev =3.89 MPa). The mortar adopted in the masonry joints was hydraulic lime-based. Standard compressive tests and three-points bending tests performed on 160x40x40 mm^3 prisms (UNI EN 1015–2-2007) provided the average compressive strengths of 4.77 MPa (st.dev =0.51 MPa) and the average flexural tensile strength of 1.85 MPa (st.dev =0.17 MPa). The haunching material has the same composition of the conglomerate adopted for the mortar joints, and its compressive strength is evaluated on cubic specimens following the UNI EN 12390 −1:2002, obtaining 12.13 MPa of compressive strength (st.dev =0.97 MPa).

The mechanical properties of masonry were assessed through the compressive testing (UNI EN 1052–1) of 3 representative masonry prisms of dimensions 500x500x110mm^3. An average compressive strength of 9.46 MPa (st.dev =1.34 MPa), an average elastic modulus of 9300 MPa (st.dev =2267 MPa) and peak strain 3.43 ‰ (st.dev =4.16e-5) were obtained. In addition, cohesion and friction angle were also determined to be c = 0.15 MPa and φ = 0.598 rad, respectively, through the methodology that will be the subject of a future publication.

The FRCM composite used in the present experimental study is made of bidirectional fabric and inorganic matrix constituted by a pozzolanic cement-based matrix.

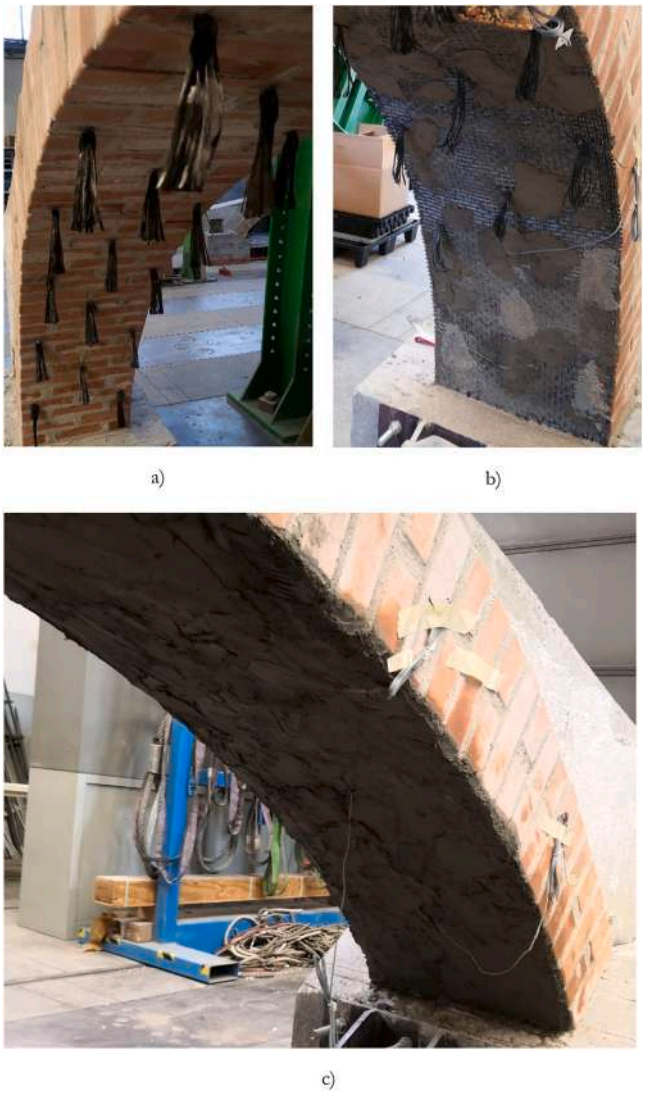

Fig. 3. Application of the strengthening system: a) Application of the spike anchors; b) application of the first layer of mortar and the fiber strip; c) application of the second layer of the matrix.

The fiber used is a carbon fiber non-impregnated with the equivalent thickness in both directions of $t_f = 0.065$ mm and with a mass density $\rho = 110$ g/m^2.

Mechanical properties of the FRCM composite were investigated thorough the mechanical characterization of the constituent materials. Experiments executed in a previous work by the authors [36] also included the characterization of tensile and shear bond strengths between the FRCM and masonry by means of pull-off and single-lap shear tests.

The average tensile strength and elastic modulus of the carbon fiber were obtained by tensile tests (ASTM D3039) and were respectively equal to 1325 MPa (st.dev =101.13 MPa) and 208 GPa (st.dev =23.35 MPa).

The matrix compressive and flexural tensile strengths were investigated on 160x40x40 mm^3 prisms (UNI EN 1015–2-2007) and were equal to 31.69 MPa (st.dev =2.32 MPa) and 6.67 MPa (st.dev =0.73 MPa), respectively.

Single-lap shear tests were performed on specimens having the same radius of curvature of the intrados of the arch specimen tested. An average debonding stress of 648 MPa (st.dev =141.8 MPa) was derived from these tests.

a)

b)

Fig. 4. a) Unstrengthened and b) Strengthened scaled masonry bridge specimen.

2.3. Test setup

An experimental campaign involved two masonry arch models with the same properties: one was tested in the unstrengthened configuration and one was strengthened at the intrados with one layer of carbon FRCM composite.

The specimens were built directly on rigid supports, able to restrain the horizontal displacement of the springings of the arch. The contrast element was anchored to the rigid floor slab before each test, ensuring that the contrasting horizontal and vertical displacement was null. The stiffness of the reaction frame system was designed to be significantly higher than the stiffness of the masonry arch bridge.

Each model was subjected to a vertical loading-unloading cycles applied at 780.7 mm from the left springing (1/4 of the span) and distributed transversely to the arch by means of a rigid steel beam. A wooden element, appropriately cut for obtaining a triangular section, was interposed between the steel beam and the arch extrados. The loading-unloading cycles, which increased in amplitude every three cycles (see Fig. 6) starting from 0.1 mm and going up to 9 mm, were imposed under displacement control using a 500 kN capacity actuator equipped with a 100 kN load cell. A preload of 1.5 kN (about the 5 % of

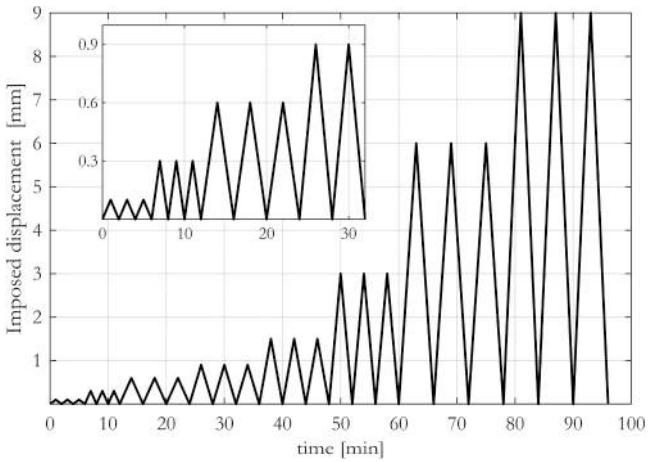

Fig. 6. Imposed displacement cycles.

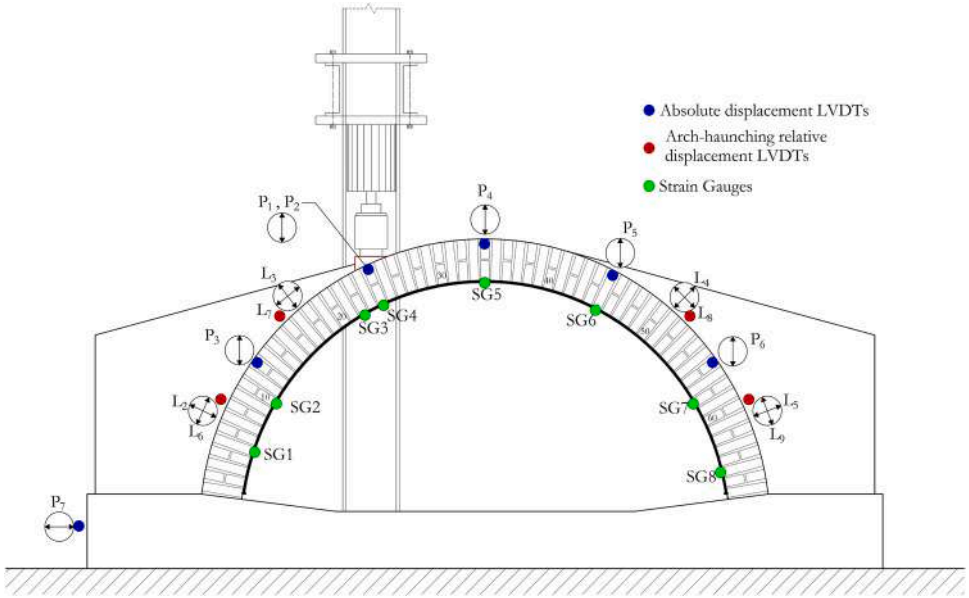

Fig. 5. Test setup.

the unstrengthened arch capacity) was applied in load control before imposing the displacement cycles.

During the tests, vertical displacements in some points of the arch were measured by means of 6 LVDTs (Fig. 5); in particular aligned to the imposed load were placed one LVDT per side, P_1 south side and P_2 north side, to investigate the displacement imposed by the actuator and eventually any transverse asymmetries. 8 LVDTs are applied on the haunching to register the relative tangential and normal displacements between the haunching and arch at the haunching-arch interface (Fig. 5). Finally, one LVDT (P7) was applied to the rigid support to investigate the horizontal displacement of the structure.

For the strengthened vault, 8 strain gauges were fixed to the central string of the carbon fiber mesh with the aim of measuring the punctual tensile strains of the fiber. The application position of the strain gauges is derived from the presumed kinematic mechanism that is supposed to occur. In particular, two strain gauges were inserted in correspondence of the point of load application since a hinge opening at the extrados was expected at this position as witnessed by numerous experimental campaigns with similar setups.

Fig. 5 reports the position of the utilized instrumentation to the strengthened specimen; the unstrengthened specimen differs from the lack of strain gauges applied to the strengthening system.

3. Tests results

This section reports the results of the experimental tests performed on the unstrengthened arch and the arch strengthened with the FRCM system, in terms of deformed shape, load-displacement curve, and analysis of damage occurring during the test. The specimens were monitored during testing by the authors with the help of cameras to detect cracks, detachments or other damage and to be able to collocate these events in the load-displacement curve. The load-displacement curves shown below refer to the load recorded by the acquisition system and the average displacement values measured by the two LVDTs positioned at the point of load application, (P1 and P2) (highlighting not the displacement impressed but the displacement that occurred in the arc).

3.1. Unstrengthened specimen

The maximum load recorded is 32.39 kN, obtained at the first cycle of 3 mm imposed, at 0.86 mm average displacement recorded by the two LVDTs P1 and P2. About 0.4 mm of residual displacement is recorded in this cycle. The peak load values recorded in the other two 3 mm imposed cycles are about 25.3 kN and 24.6 kN. In these cycles, it is possible to observe stiffness degradation in the load-displacement curve due to the activation of the 4-hinge mechanism (Fig. 7) at the peak load. In the first cycle of 6 mm imposed, an increase in load is shown, with maximum value of 28.15 kN recorded at 3.37 mm. In this cycle 4.9 mm of maximum recorded displacement is reached while maintaining 0.4 mm of residual displacement.

Next cycles show a further reduction in stiffness in the initial loading section and a change in slope at about 2.5 mm recorded until the maximum load of about 22.6 kN and 20.9 kN and, when an increase in residual displacement is recorded, up to 0.65 mm even if the maximum displacement remains constant. The last load cycle of the test, with 9 mm imposed-displacement, shows a similar behavior to the previous two cycles in terms of initial stiffness, change of slope and maximum load (20.73 kN) but differs in the post-peak phase, in which there is a decrease in the recorded load up to 18.1 kN at the maximum recorded displacement of 7.98 mm. The test was stopped because of the decrease in the load respect to the peak of about 45 %.

Fig. 9 shows the damage stages of the vault and Fig. 8 places these stages in the load-displacement curve. The first crack (A1) was detected between the arch and the west haunching during the first cycle with 1.5 mm of imposed displacement. The peak load coincides with the opening of 4 hinges mechanism (B1); the westernmost hinge is localized by cracks between bricks and mortar joints from courses 15 to 17 and by a crack along the bricks from course 14 to 15, indicative of a high compression state. The other hinges at this stage are represented by crack openings between the brick and mortar joint and between the haunching and support. During the first 6-mm cycle imposed by the actuator, sliding along the cracks parallel to the pre-existing mortar joints at the westernmost hinge is detected. The shear strength of the involved section is affected by the high compression, resulting in a combined failure of sliding and crushing. In the unloading phase of the first 6-mm cycle, the masonry affected by sliding returns to its initial position. In the next 6-mm cycles, such a loading-unloading behavior recurs. In the final loading cycle, a crack opening between the mortar and the brick between course 34 and 35 is detected. In this cycle, the sliding displacement described above increases in amplitude and, in the unloading phase, the masonry does not return to its original position, thus showing plastic displacement. A total of 22 loading-unloading cycles were performed.

3.2. Strengthened specimen

The test performed on the strengthened arch shows the linear behavior in the first load cycles, in which a maximum of 0.9 mm of displacement is imposed, reaching a value of about 17 kN. During the

Fig. 7. Deformed shape of the unstrengthened arch at the load peak: activation of the principal mechanism (B1).

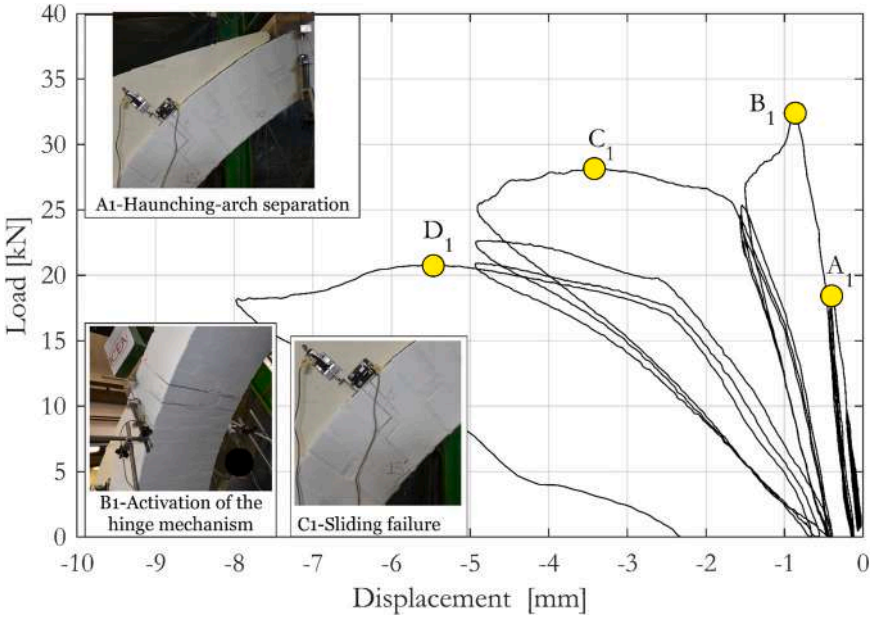

Fig. 8. Load-displacement curve with the principal damage phases.

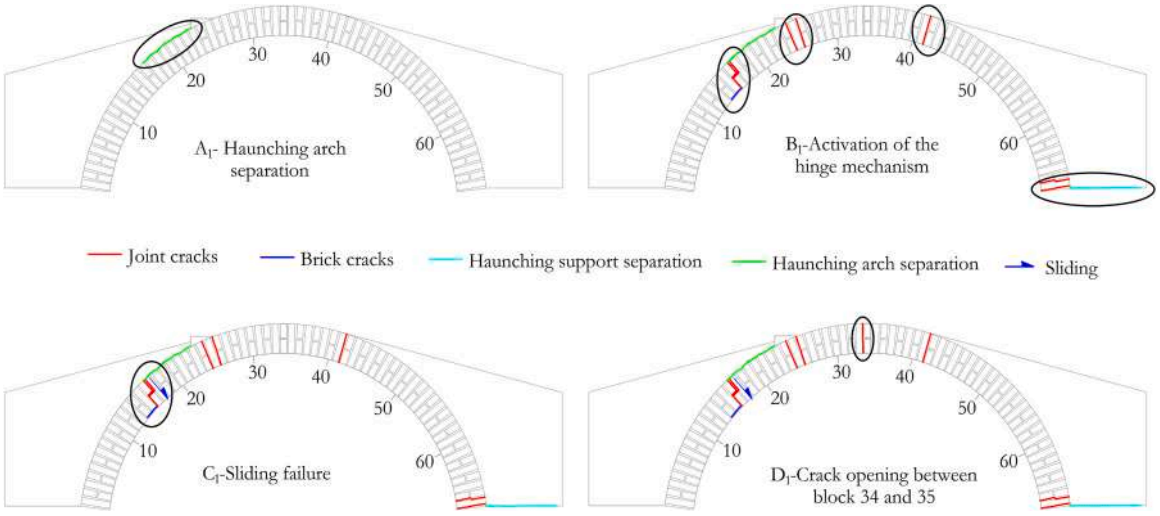

Fig. 9. Damaging of the unstrengthened arch, during the test.

first cycle of 1.5 mm imposed, a nonlinear behavior is registered with a degradation of stiffness and an increase in residual displacement up to a value of 0.25 mm versus 0.77 mm of maximum displacement detected. In the cycle with the next higher amplitude, the specimen manifests a local peak at 28.99 kN and 0.85 mm corresponding to the activation of the 4-hinge mechanism, which leads to a decrease in the global stiffness, until the peak value of the cycle of 44.80 kN at 1.90 mm of recorded displacement. The peak load of the test was recorded at 2.39 mm and is equal to 53.86 kN. In this cycle, after the peak load, there is a decrease in the recorded load and a constant-load behavior until the recorded displacement value of 4.77 mm. The residual displacement value is 1.57 mm. The next two cycles, which have the same imposed displacement amplitude of the peak load cycle, show in the loading phase a change in slope of the load-displacement curve at about 2 mm recorded, and reach the load of 39.5 kN and 37.6 kN respectively. The first cycle with the maximum displacement amplitude shows a behavior similar to the previous two cycles in the loading part up to a displacement of 5.28 mm, at which follows firstly a decrease and then an increase in the recorded load up to the peak of 40.3 kN. A second decrease in load is detected until reaching the maximum displacement of 7.88 mm with a load of 38.12 kN. The residual displacement in this cycle is 3.08 mm. The last two cycles replicate the second and third cycles of previous displacement amplitude, showing a lower stiffness and slope change at about 4 mm.

Fig. 12 shows the damage stages detected in the strengthened arch during the test and, in Fig. 11, these main stages are indicated in the load-displacement curve.

Similarly to the test performed on the unstrengthened arch, the first crack (A2) is detected between the arch and the haunching on the west side at the first 0.9 mm imposed displacement cycle. In this case, a crack is also formed in the haunching in the area near the point of load application where the haunching section is thinner. During the first 3 mm imposed cycle, the opening of the 4-hinge mechanism with similar configurations to those observed for the unreinforced arch (B2) can be noted and a crack between the arch and the strengthening system appears from course 23 to course 30. This step is visualized in the load-displacement curve as a change in global stiffness. From this step to the peak load, which occurs in the first 6 mm imposed cycle (B*2), the

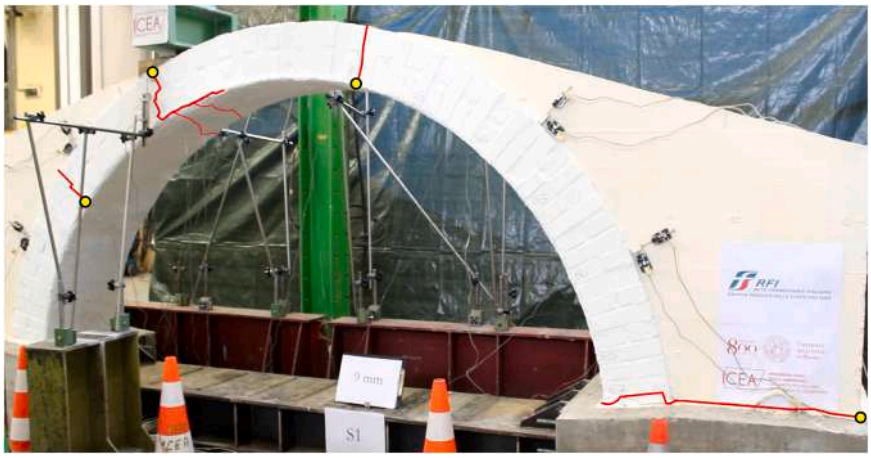

Fig. 10. Deformed shape of the strengthened arch at 9 mm imposed displacement.

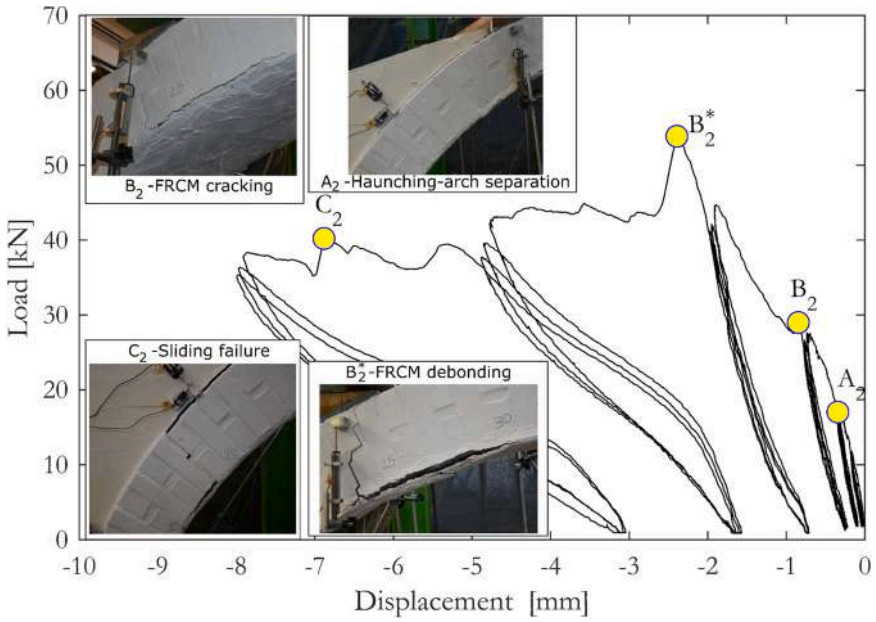

Fig. 11. Load-displacement curve vs the points of activation of the principal mechanisms.

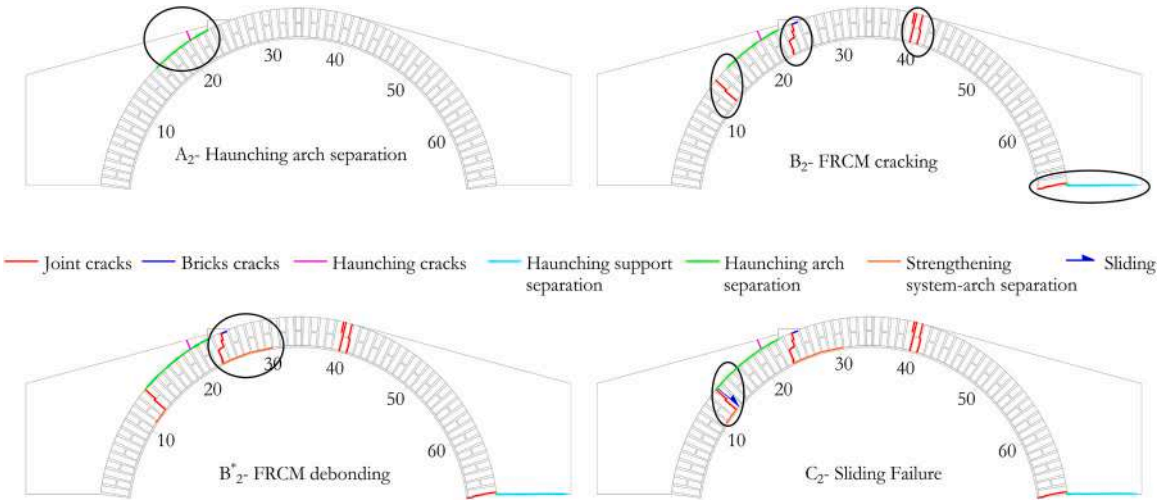

Fig. 12. Damaging of the strengthened arch, during the test.

fiber is active and contributes to the overall response of the structure. At the peak, debonding of the strengthening system and widening of the crack between the arch and the strengthening system occurs. The westernmost hinge shows cracking between the arch and the strengthening system at courses 12 and 13. In the first 9-mm imposed displacement cycle, sliding (C2) occurs at the interfaces between courses 13 and 14. Consistently with the test on the unstrengthened arch, high compressive forces are localized in the westernmost hinge, leading to brick failure detected on the north side. In the unloading phase, the portion affected by sliding does not return to its initial position, but instead residual displacement is recorded.

4. Discussion of results

In this section, the results obtained during the experimental tests are presented and analyzed by comparing the detected displacements, load-displacement graphs, deformed configurations and kinematic mechanisms highlighted by the two vaults. The contribution of the strengthening system is presented by illustrating the deformations developed by the fiber during the peak load.

4.1. Comparison between the unstrengthened and the strengthened arches

Fig. 13 shows the comparison between the unstrengthened arch and the FRCM- strengthened arch in terms of the load-displacement curve. The initial stiffnesses, highlighted in the unstrengthened specimen as the curve before the peak load (B1) and in the strengthened specimen as the section before the change in slope that occurs at about 28 kN (B2), are almost equal. The explanation is that, in the elastic phase where the hinge mechanism has not yet formed, the strengthening system does not affect the stiffness of the structure and the overall response is equal. The B1 and B2 stages occur at an average detected displacement that is almost equal (0.85 mm for the strengthened and 0.86 mm for the unstrengthened). In terms of the recorded load, the values of these two conditions are comparable (28.99 kN vs 32.39 kN). For the strengthened arch, the B2 point indicates fiber activation, which allows the vault to reach the peak load value at a detected displacement of 2.39 mm.

With regard to the recorded peak force, attention is drawn to the ratio between the two maximum load values of 1.66, which can be interpreted as the index of strengthening system effectiveness in the arch. It is important to clarify that these results are obtained from a 1:2 scale bridge, and the extrapolation of their effectiveness to full-scale bridges may not be linear. In particular, the phenomenon of 'scale effect', which has not yet been extensively studied in the literature, can occur when the dimensions of the arch model vary. In this work is possible to observe a less pronounced strengthening system effect compared to the tests performed on small scale stand-alone masonry arches [30]. This is due to two factors: differences in geometric ratios and dimensions, and the effect of haunching, which increases the normal stress within the arch.

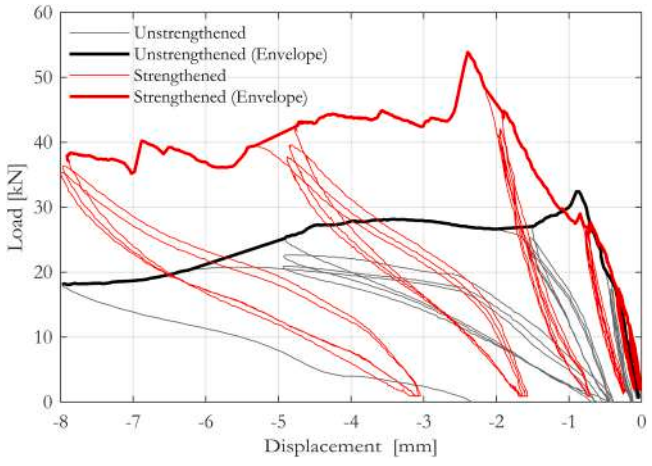

Fig. 13. Comparison between the results of the unstrengthened and strengthened arches.

Both arches show a decrease in the recorded load after the peak phase, which is followed by a load-almost-constant section up to about 5 mm of detected displacement. After this value, the load decreases and both specimens reach 8 mm of detected displacement although with different loads: 18.1 kN for the unstrengthened arch and 38.1 kN for the strengthened one (ratio of 2.1). This difference in residual load is due to the contribution of the fiber, which is also active in the post-peak phase.

In Fig. 14, the displacements detected by the vertical LVDT applied to the unstrengthened and strengthened arch are presented. It is possible to compare the deformed configurations at the peak load point (B1 and B*2) and at the post-peak peak (C1 vs C2). These points were chosen to highlight the complete activation of the 4-hinge mechanism; indeed, as it can be observed in the graph, the displacements are consistent with the mechanisms described above. The displacement values are expressed as a ratio with respect to the maximum displacement detected for each specimen at both steps considered. The configuration at the peak load for the two specimens is different: in the case of the unstrengthened specimen, the LVDT P5 shows a relative value of 0.05 while, for the strengthened arch, this is equal to 0.38. This fact indicates how, for the unstrengthened arch, the peak load coincides with the activation of the 4-hinge mechanism; meanwhile, the strengthened arch, before the peak load has already fully formed the 4-hinge mechanism. In the post-peak phase, the two configurations overlap, highlighting that once the mechanism has fully developed, the structures exhibit the same behavior.

The unstrengthened arch exhibits at the peak load, as already stated, a 4-hinge mechanism, deforming according to the representation in Fig. 16 in the loading phases and closing the hinges in the unloading phases. With the shear-compression sliding phenomenon, coinciding with the C1 damage phase, the above mechanism evolves into a 3-hinge mechanism and a roller.

Stage D1 coincides with the opening of a crack between course 33 and 34 between the mortar joint and the brick and with the closure of the hinge between the 24th and the 26th blocks. In this phase, the slippage of the west -side block stops and a hinge can be identified in the slippage joint section at the extrados, in a position shifted inward to the arch for the residual slip that occurred. The new mechanism that is formed is a 4-hinge mechanism, in which the easternmost hinges and the hinge between courses 41 and 42 remain unchanged from the main mechanism, while the central hinge between block 33 and 34 results at the intrados.

The mechanism manifested by the strengthened arch at the peak load is, as for the unstrengthened arch, a 4-hinge mechanism (Fig. 17). The fibers can be considered active at the intrados of the 23rd/25th block hinge due to the opening of the hinge. At the easternmost hinge, it is not possible to observe the activation of the tensile fiber since, in this experimental campaign, the anchorage between support and strengthening system was not considered. The secondary mechanism C2 exhibits sliding in the westernmost hinge section as for the unstrengthened case, evidencing in strengthening peeling in the 12th /13th blocks.

Fig. 18 shows the location of the strain gauges, which are applied to investigate the punctual strain in tension of the carbon fiber during the test. Since the fiber contributes to the overall behavior of the structure when tensile strain occurs at the intrados of the vault, the results highlighted by strain SG3 and SG4 are considered relevant. The strains in compression, which show smaller values than those observed in tension, are therefore not significant for the purpose of investigating the mechanical behavior of the fiber since the fiber can be considered not active in compression. Fig. 19 presents the crack pattern at the intrados of the arch at the load application location, detected between the two strain gauges mentioned above. The fact that SG3 shows a higher strain value

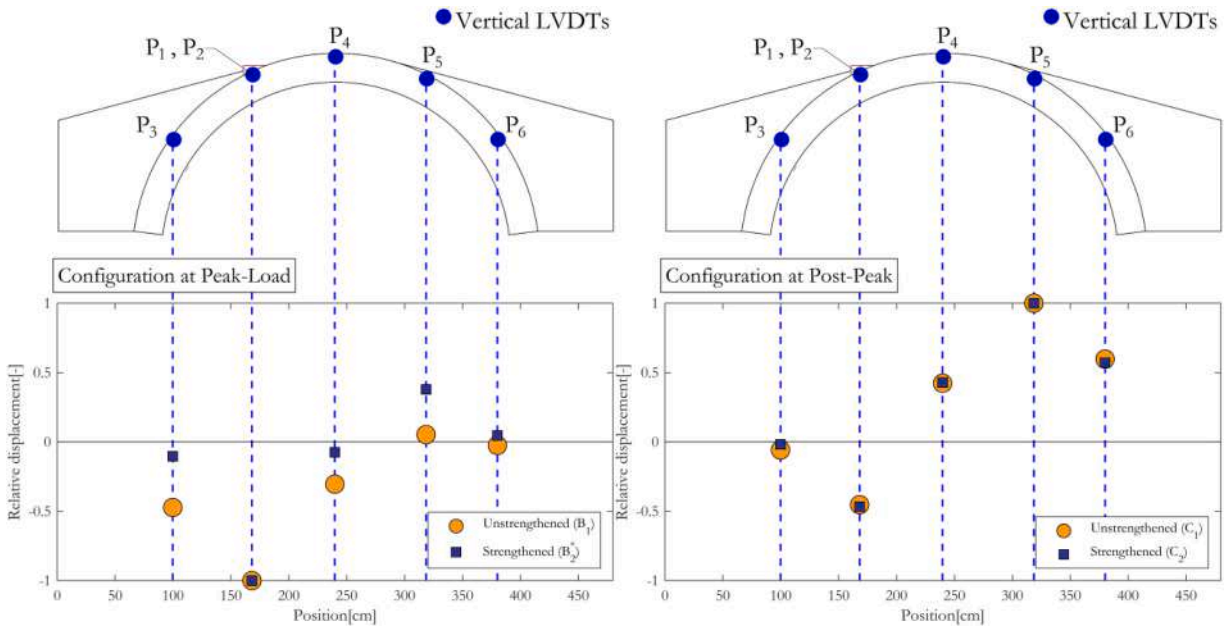

Fig. 14. Comparison between the vertical displacements registered by the vertical LVDTs at the peak load (left) and in the post peak phase(right) for the strengthened and unstrengthened arch, expressed as the ratio of the vertical displacement and maximum amplitude of the vertical displacement registered for the specimen at the phase selected. The steps represenfor the unstrengthenedarch are B_1 and C_1 reffering to Fig. 8 meanwhile B^*_2 and C_2 for the strengthened ne referring to Fig. 11.

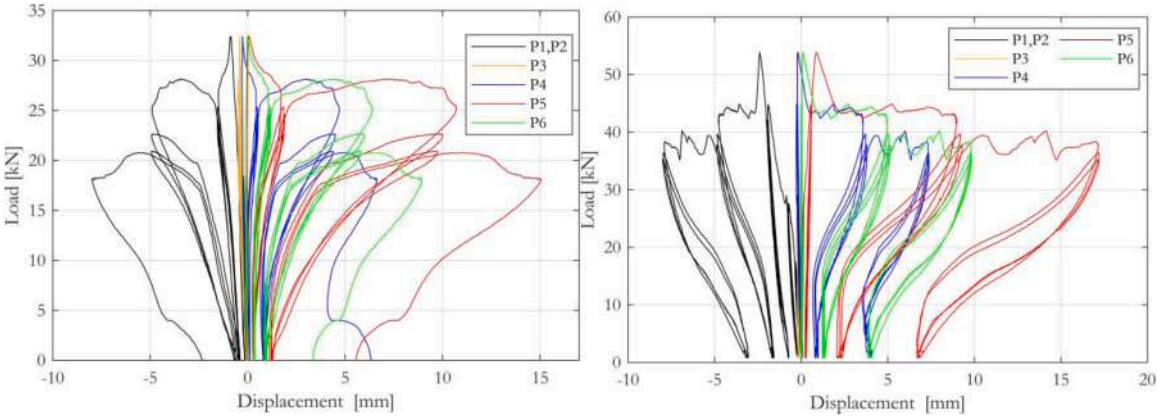

Fig. 15. Displacement registered by the vertical LVDT for the unstrengthened arch (left) and strengthened one.

than SG4 is due to its closer proximity to the crack with respect to the other one.

Multiplying the strain of SG3 at the load-peak condition by the elastic modulus of the fiber results in a stress of about 434 Mpa. Considering the telescoping effect, the fact that SG3 is not precisely on the hinge crack, so the strain gauges didn't register the maximum strain value at the peak load, the stress value obtained results close to the average maximum stress (648 Mpa) obtained from the adhesion tests [36].

Fig. 20 reports the relative displacements between the arch and the haunching detected by the specific LVDTs vs the load recorded during the test. The only relevant displacements are the ones obtained from L3, positioned normally with respect to the interface, and the L7, positioned parallel to it, both placed near the westernmost hinge that developed sliding mechanism. In the Fig. 21 the displacements are compared to the average displacement detected by LVDTs P1 and P2, expressed during the test time. The reported data confirm the structural behavior anticipated in the previous chapter. These LVDTs start to detect the displacement in both normal and tangential directions at the B2 damage phase, coherently with the activation of the 4-hinges mechanism. In these cycles, it is possible to observe a peak of the displacement detected by the haunching-arch LVDTs at the maximum imposed displacement and a plastic displacement of 0.24 mm for both strain gauges. In cycles where 6 mm of displacement is imposed, the displacements of L3 and L7 increase in amplitude. The tangential displacement reaches 2 mm and a residual displacement of 0.74, maintaining the same behavior for these 3 load cycles; the normal displacement increases at each peak both the maximum value and the residual value, indicating the forewarning for the sliding mechanism. In the 9 mm imposed displacement cycles, the tangential displacement trend remains almost unchanged from the previous phase while L3 records peaks up to 10 mm with a maximum residual displacement of 8.47 mm, due to the complete activation of the sliding mechanism.

5. Design procedure of FRCM strengthened masonry bridges

Knowing the positions of the hinges in the condition when the structure starts its kinematic mechanism (which, in the present case, coincides with the peak load), through limit analysis, it is possible to

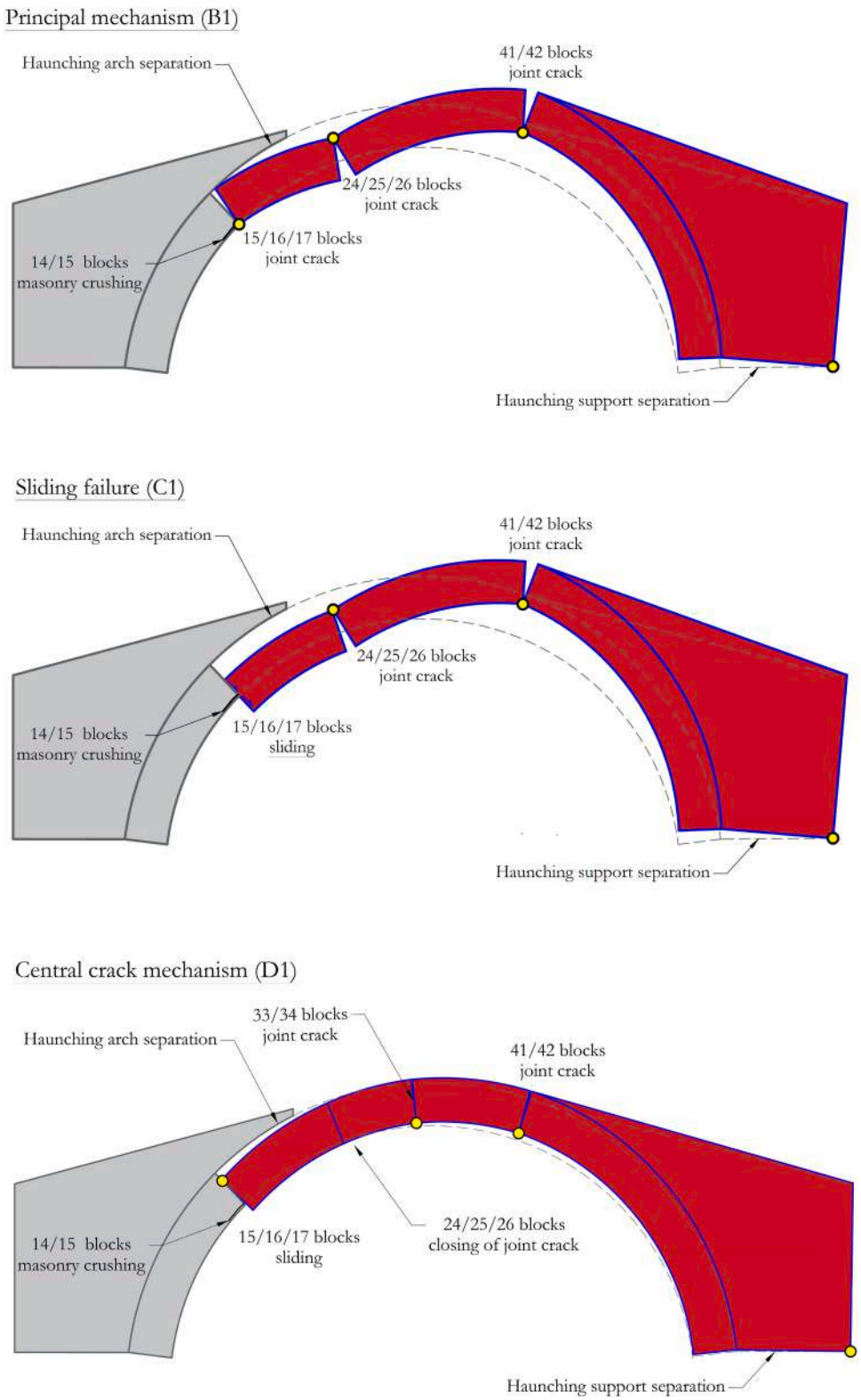

Fig. 16. Simplified visualization of the principal mechanisms for the unstrengthened arch B1, C1, and D1 referring to the load -displacement curve in Fig. 8.

obtain the limit load. Having defined the collapse mechanism presented in Fig. 22, it is possible to obtain the virtual displacement diagram in order to calculate the limit load value, in the hypothesis that sliding between blocks is not permitted.

Starting from the simplified stress-strains diagrams shown in the (Fig. 23 top), the limit analysis is conducted under the additional assumption that the materials exhibit rigid-plastic behavior. The assumption for the masonry is the use of a constitutive law in compression with zero tensile strength resistance. Meanwhile the FRCM composite results active exclusively under tension, developing the maximum stress of $\alpha\sigma^*$, where α is a amplification coefficient and σ^* is the maximum stress observed in the shear lap tests. Therefore, the force

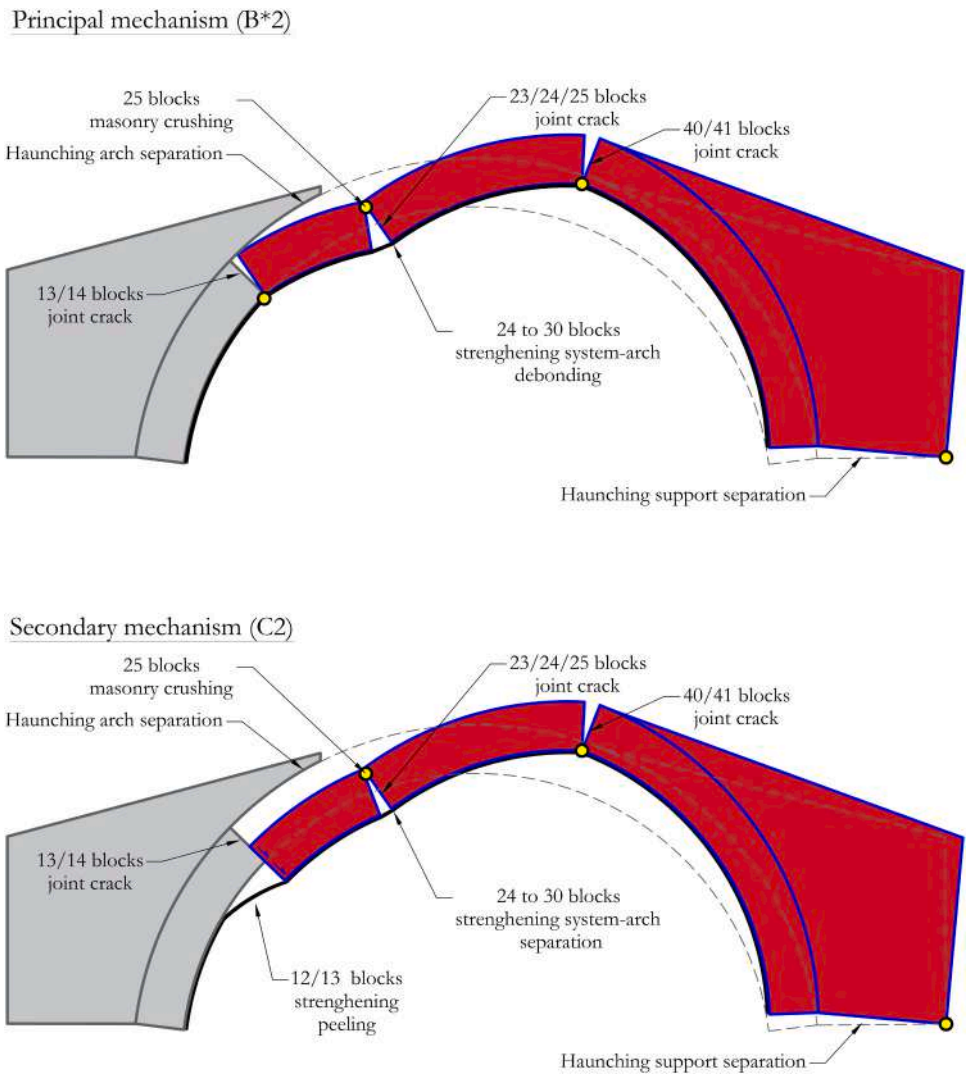

Fig. 17. Simplified visualization of the principal mechanisms for the strengthened arch, B* 2 and C2 referring to the load -displacement curve in Fig. 11.

configuration at the extrados and intrados hinges can be derived (Fig. 23 bottom). The additional contribution provided by the FRCM composite can be observed in the hinge located under the load application point. The opening of the arch at the intrados allows the development of tensile forces in the FRCM composite, enabling the activation of the fibers.

Applying the Virtual Work Theorem:

$$L_e = L_i$$

$$\Sigma W_k \delta_k + \lambda P \quad \delta_P = \Sigma M_{Fi} \Delta\varphi_i + \Sigma M_{Cr} \Delta\varphi_r \tag{1}$$

Where:

i = 1, 2,.n.
j = 1, 2,.m.
r = 1,2,., n + m.
n = number of hinges with active fibers.
m= number of hinges with inactive fibers.
r = m+n = total number of hinges

$$M_{Fi} = T_F \quad (s_i - 2d_i + a) \quad T_F = A_F \alpha \sigma^* \tag{2}$$

$$M_{Cr} = N_r(d_r) \quad N_r = f_m s_r \quad (2d_r) \tag{3}$$

From Eq. 1 derives λP once known f_m and $\alpha\ \sigma^*$.

Imposing $F_u^{EX} = F_u^{LA}$, where F_u^{EX} is the maximum value obtained experimentally and F_u^{LA} is the value obtained from the procedure just described, derives the value of α equal to

$$\alpha = 1.16$$

The coefficient alpha is greater than 1, which can be considered a positive result. As demonstrated by other studies in the literature, the maximum deformation observed in tests on reinforced elements is generally greater than the failure stress and strain obtained from direct shear tests.

The FRCM system was designed based on the results obtained from direct shear tests (single shear lap tests) to achieve a structural capacity increase of over 60 %. However, the limitations of this strengthening system concern the potential fatigue behavior of masonry bridges strengthened with FRCM, a phenomenon that has not been extensively studied and for which there is insufficient academic literature. This type of strengthening system significantly enhances the flexural strength of the arch; however, the increase in the shear strength of the arch provided by it is negligible. Consequently, in cases where failure mechanisms involve sliding phenomena, the effectiveness of the FRCM may be limited [68,69]. It is, therefore, recommended to verify that the arch being strengthened does not develop shear collapse. Since in the strengthened arch occurs changes in the trend of the pressure line respect to the unstrengthened vault, it is possible to have high shear forces. Therefore, a shear check is performed in a simplified way in each section to verify that before the maximum load is reached at the

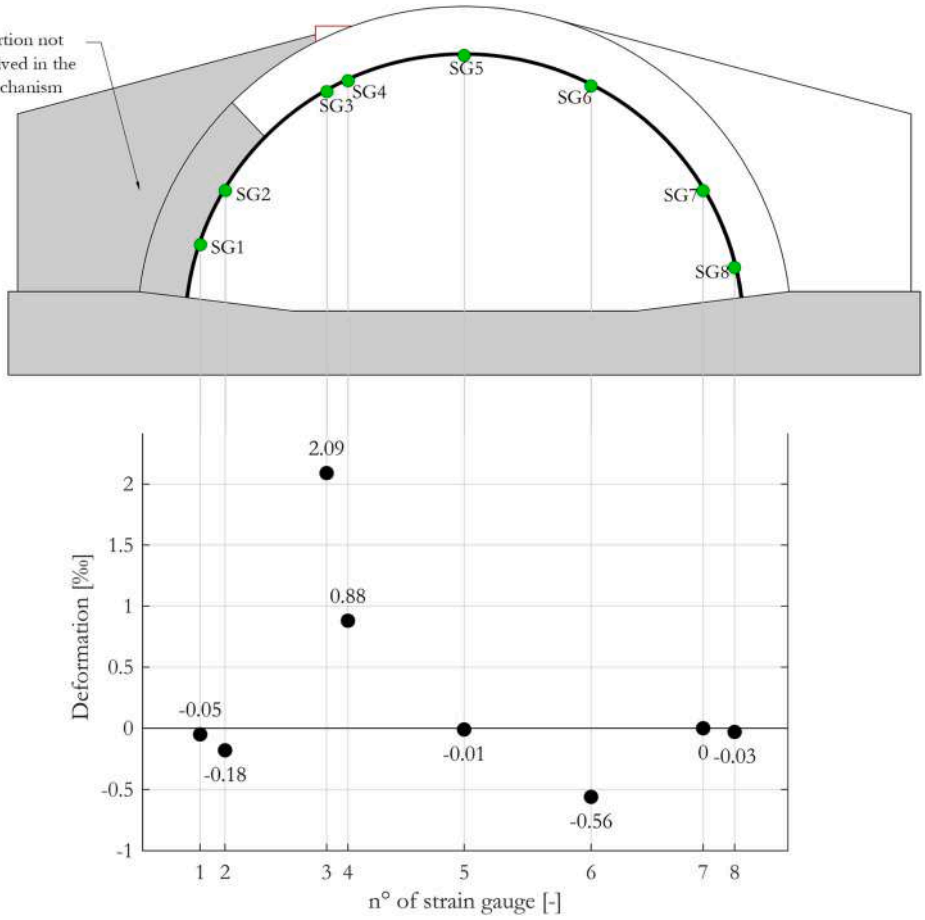

Fig. 18. Application position of the strain gauges (top) and strain registered by the strain gauges in correspondence of the peak load.

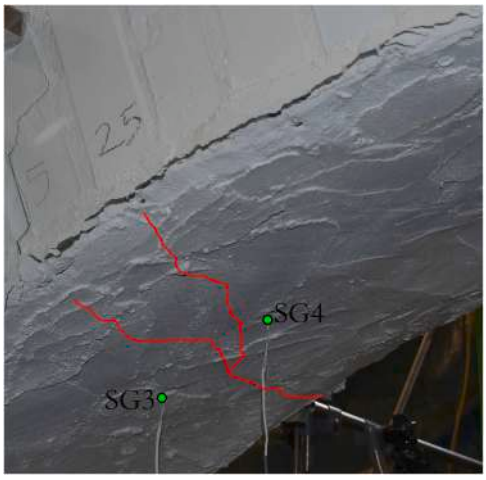

Fig. 19. Crack pattern on the intrados under the point of application of the load and position of the strain gauges SG3 and SG4 at the B2 * damaging phase.

activation of the mechanism, shear collapse does not occur. The shear strength is given by:

$$V_{RD} = \mu N_i + V_0 \tag{4}$$

Where μ is the friction coefficient and V_0 is the cohesive strength.

If for every section:

$$V_{ED} \leq V_{RD} \tag{5}$$

The limit load obtained from the previously illustrated procedure is confirmed; otherwise, T_F is reduced until the condition is assured.

6. Conclusion

This paper presents and discusses the results obtained from an experimental campaign aimed at investigating the effectiveness of FRCM strengthening system applied to the intrados of masonry vaults. For this purpose, two vaults with the same geometrical dimensions, one unstrengthened and the other strengthened with FRCM system composed of carbon fiber and cementitious matrix, were produced and tested through quasi-static load cycles with eccentric loading. In order to reproduce the real behavior of masonry bridges present in the Italian railway network, the haunching is introduced as a conglomerate and the span was fixed of about 3 m.

The experimental results indicate an increase in load-carrying capacity of approximately 1.66 with respect to the unstrengthened case, without variation in the initial stiffness, and an increase in the residual load carrying capacity of 2.10.

The experimental behavior of the arches is characterized by the formation of the typical 4-hinge mechanism, which is followed in both cases by the sliding of a previously cracked section that leads to the evolution of the mechanism into 3-hinges and a roller. The unstrengthened arch shows, at the last load cycle the rotation, of the block subject to slip and the closure of a hinge, a phenomenon that re-establishes the 4-hinge mechanism with a variation compared to the previous hinge configuration.

LVDTs monitoring vertical displacements along the arch enable the confirmation of the visually observed collapse mechanisms. LVDTs placed at the interface between the arch and the haunching that detect

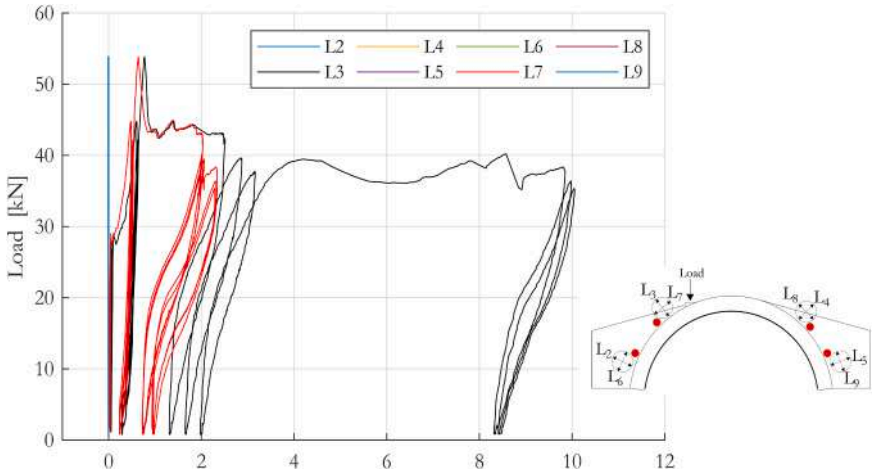

Fig. 20. Load registered during the test vs Displacement of the Tangential (L2 to L5) and the normal (L6 to L9) LVDTs.

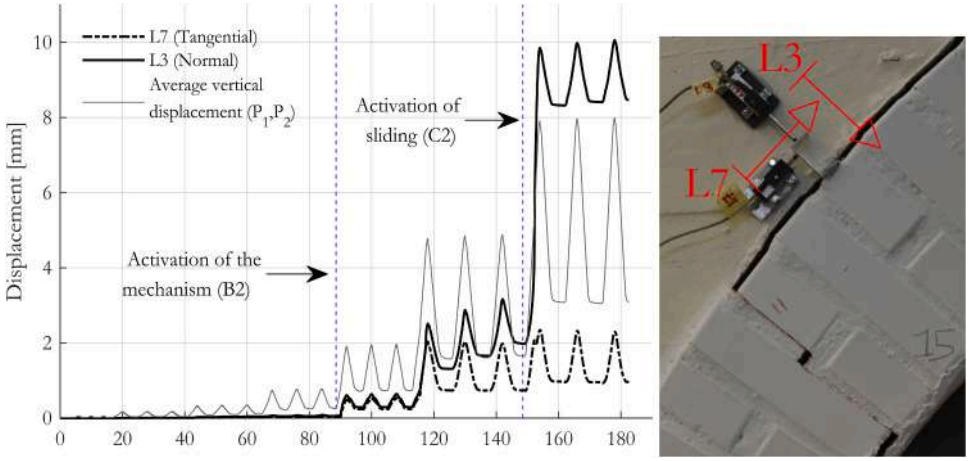

Fig. 21. Displacement of the Tangential (L7) and the normal (L3) LVDTs respect to the arch-haunching interface vs the time.

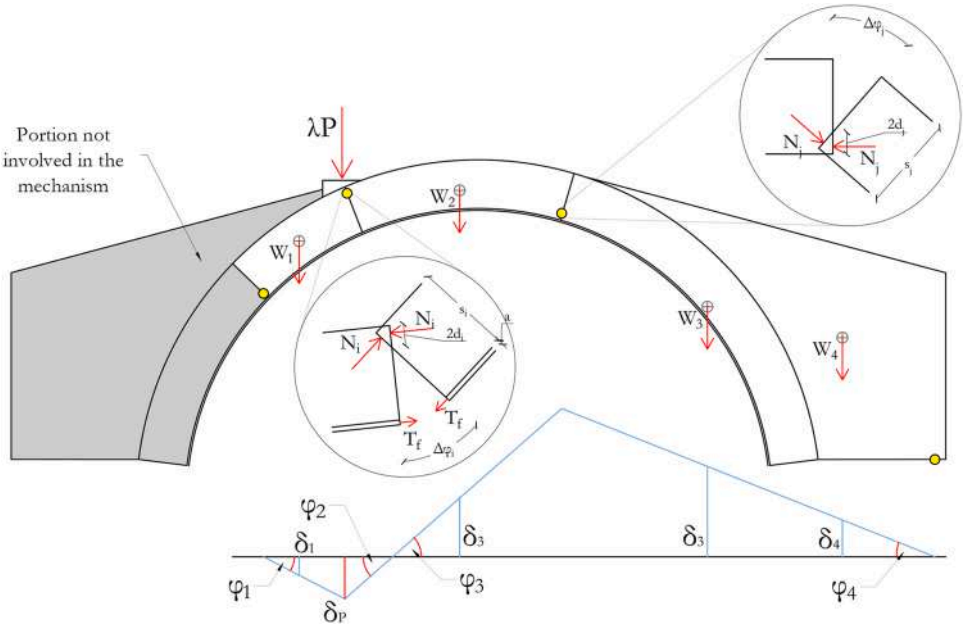

Fig. 22. Virtual displacement diagrams applied to the masonry arch in order to calculate the limit load value.

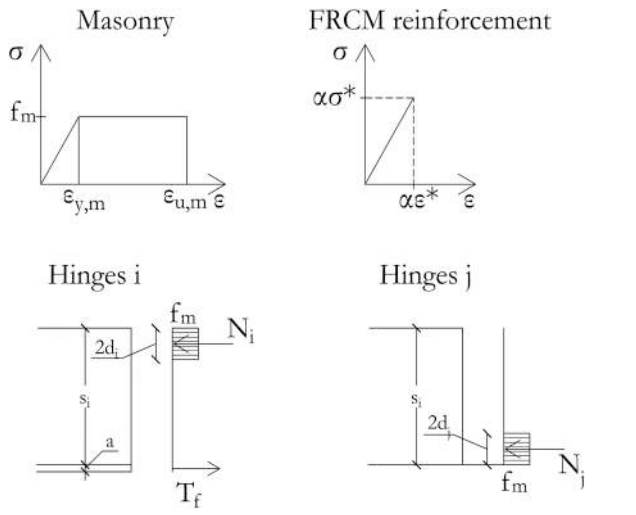

Fig. 23. Constitutive laws for the Masonry and the FRCM (top) and force configuration for extrados and intrados hinges (bottom).

the relative displacements between these two elements, allowing in the case of the strengthened arch to accurately characterize the sliding mechanism described above. The strain gauges applied in the strengthening system allow to detect fiber strains and confirm the degree of fiber efficiency, which results comparable to the output obtained from the previously executed experimental campaign aimed to investigate the behavior of FRCM system applied to strengthened curved masonry specimens [54]. In particular, the fiber shows its best effectiveness in the hinge under the load application point, on which intrados tensile strain occurred. Due to the time and cost constraints, it is not possible to produce a large number of arch models. Consequently, it is not feasible to estimate the variance of the results obtained. However, in this case, the results derived from the analytical approach are useful in providing a certain degree of reliability to the experimental outcomes.

The just-mentioned conclusions confirm that the FRCM system is a valid technique for the strengthening of masonry bridges, as it can provide a significant increase in terms of load-carrying capacity. However, further investigations are required in order to replicate the application in situ of this system. In particular, the presence of abutment will permit to extend the application of the FRCM system under the base of the arch and to cover the intrados of the arch-support hinge developed in the present experimental tests (easternmost hinge). This peculiarity will permit to introduce another point of activation of the fiber, hypothetically increasing even more the load carrying capacity of the bridge.

CRediT authorship contribution statement

Franco Iacobini: Validation, Resources. **Andrea Vecchi:** Validation, Resources, Conceptualization. **Francesco Iodice:** Validation, Resources, Project administration, Conceptualization. **Domenico Ricci:** Validation, Project administration. **Paolo Zampieri:** Writing – review & editing, Writing – original draft, Supervision, Project administration, Methodology, Investigation, Funding acquisition, Formal analysis, Data curation, Conceptualization. **Riccardo Piazzon:** Writing – review & editing, Writing – original draft, Formal analysis, Data curation. **Davide Santinon:** Writing – review & editing, Writing – original draft, Formal analysis, Data curation. **Lorenzo Hofer:** Methodology, Formal analysis. **Klajdi Toska:** Methodology, Formal analysis. **Flora Faleschini:** Methodology, Formal analysis. **Carlo Pellegrino:** Supervision, Resources, Funding acquisition.

Declaration of Competing Interest

The authors declare no conflict of interests.

Acknowledgements

F.R.C.M. composite used in the experiments were provided by G&P Intech. The academic authors gratefully acknowledge support from RFI S.p.A. within the research project 'Valutazione sperimentale del rinforzo con materiale composito a base cementizia di archi in muratura' CIG ZC22CD2337 - CUP J57I12000690001."

Data Availability

No data was used for the research described in the article.

References

[1] Da Porto F, Tecchio G, Zampieri P, Modena C, Prota A. Simplified seismic assessment of railway masonry arch bridges by limit analysis. Struct Infrastruct Eng 2016;12(5):567–91. https://doi.org/10.1080/15732479.2015.1031141.
[2] Zampieri P, Tecchio G, da Porto F, Modena C. Limit analysis of transverse seismic capacity of multi-span masonry arch bridges. Bull Earthq Eng 2015;13(5):1557–79. https://doi.org/10.1007/s10518-014-9664-3.
[3] Zampieri P, Zanini MA, Modena C. Simplified seismic assessment of multi-span masonry arch bridges. Bull Earthq Eng 2015;13(9):2629–46. https://doi.org/10.1007/s10518-015-9733-2.
[4] Zampieri P, Zanini MA, Faleschini F. Derivation of analytical seismic fragility functions for Common Masonry Bridge types: Methodology and application to real cases. Eng Fail Anal 2016;68:275–91. https://doi.org/10.1016/j.engfailanal.2016.05.031.
[5] Zampieri P, Perboni S, Tetougueni Denis, Pellegrino C. C. Different approaches to assess the seismic capacity of masonry bridges by non-linear static analysis (art. no) Front Built Environ 2020;6:47. https://doi.org/10.3389/fbuil.2020.00047.
[6] Zampieri P, Tetougueni CD, Pellegrino C. Nonlinear seismic analysis of masonry bridges under multiple geometric and material considerations: Application to an existing seven-span arch bridge. Structures 2021;34:78–94. https://doi.org/10.1016/j.istruc.2021.07.009.
[7] Zampieri, P., Zanini, M.A., Faleschini, F., Hofer, L., Pellegrino, C. Failure analysis of masonry arch bridges subject to local pier scour Engineering Failure Analysis, 79, pp. 371–384.DOI: 10.1016/j.engfailanal.2017.05.028.
[8] Scozzese F, Tubaldi E. Dall'Asta A. Damage metrics for masonry bridges under scour scenarios (art. no.) Eng Struct 2023;296:116914. https://doi.org/10.1016/j.engstruct.2023.116914.
[9] Scozzese F, Ragni L, Tubaldi E, Gara F. Modal properties variation and collapse assessment of masonry arch bridges under scour action (art. no) Eng Struct 2019;199:109665. https://doi.org/10.1016/j.engstruct.2019.109665.
[10] Tubaldi E, Macorini L, Izzuddin BA. Three-dimensional mesoscale modelling of multi-span masonry arch bridges subjected to scour. Eng Struct 2018;165:486–500. https://doi.org/10.1016/j.engstruct.2018.03.031.
[11] Giamundo V, Lignola GP, Maddaloni G, da Porto F, Prota A, Manfredi G. Shaking table tests on a full-scale unreinforced and IMG retrofitted clay brick masonry barrel vault. Bull Earthq Eng 2016;14(6):1663–93. https://doi.org/10.1007/s10518-016-9886-7.
[12] Marini A, Belleri A, PretiM, Riva P, Giuriani E. Lightweight extrados restraining elements for the anti-seismic retrofit of single leaf vaults. ISSN 0141-0296 Eng Struct 2017;141:543–54. https://doi.org/10.1016/j.engstruct.2017.03.038.
[13] Ramaglia G, Lignola GP, Balsamo A, Prota A, Manfredi G. Seismic Strengthening of Masonry Vaults with Abutments Using Textile-Reinforced Mortar (art. no) J Compos Constr 2017;21(2):04016079. https://doi.org/10.1061/(ASCE)CC.1943-5614.0000733.
[14] Carfagnini C, Baraccani S, Silvestri S, Theodossopoulos D. The effects of in-plane shear displacements at the springings of Gothic cross vaults. Constr Build Mater 2018;186:219–32. https://doi.org/10.1016/j.conbuildmat.2018.07.055.
[15] Zampieri P, Piazzon R, Niero L, Pellegrino C. Damaged masonry arch bridges strengthened with external post-tensioning: Experimental and numerical results. Engineering Structures 2024;318:117929. https://doi.org/10.1016/j.engstruct.2024.117929.
[16] Firat FK, Kayabaşı MS. Investigation of tie-rod connection types on stone masonry arches. ISSN 2352-0124 Structures 2022;45:2185–97. https://doi.org/10.1016/j.istruc.2022.10.044.
[17] Ural A, Fırat FK, Tuğrulelçi Ş, Kara ME. Experimental and numerical study on effectiveness of various tie-rod systems in brick arches. ISSN 0141-0296 Eng Struct 2016;110:209–21. https://doi.org/10.1016/j.engstruct.2015.11.038.
[18] Calderini C, Lagomarsino S, Rossi M, et al. Shaking table tests of an arch-pillars system and design of strengthening by the use of tie-rods. Bull Earthq Eng 2015;13:279–97. https://doi.org/10.1007/s10518-014-9678-x.
[19] Klusáček L, Nečas R, Požár M, Pěkník R, Svoboda A. Transverse prestressing and reinforced concrete as the key to restoration of masonry arch bridges. ISSN 0141-0296 Eng Struct 2021;245:112898. https://doi.org/10.1016/j.engstruct.2021.112898.
[20] Gattesco N, Boem I. Review of experimental tests and numerical study on masonry vaults reinforced through fiber-reinforced mortar coating. Bull Earthq Eng 2019;17:4027–48. https://doi.org/10.1007/s10518-019-00619-y.

[21] Zampieri P, Simoncelo N, Tetougueni CD, Pellegrino C. A review of methods for strengthening of masonry arches with composite materials. Eng Struct 2018;171:154–69. https://doi.org/10.1016/j.engstruct.2018.05.070.

[22] Borri A, Casadei P, Castori G, Hammond J. Strengthening of Brick Masonry Arches with Externally Bonded Steel Reinforced Composites. J Compos Constr 2009;13:468–75. https://doi.org/10.1061/(ASCE)CC.1943-5614.0000030 (doi).

[23] Gioffré M, Vincenzini A, Cavalagli N, Gusella V, Caponero MA, Terenzi A, Pepi C. A novel hemp-fiber bio-composite material for strengthening of arched structures: Experimental investigation. ISSN 0950-0618 Constr Build Mater 2021;308:124969. https://doi.org/10.1016/j.conbuildmat.2021.124969.

[24] Oliveira D, Basilio I, Lourenco P. Experimental Behavior of FRP Strengthened Masonry Arches. J COMPOS CONSTR - J COMPOS CONSTR 2010;14. https://doi.org/10.1061/(ASCE)CC.1943-5614.0000086.

[25] Rovero L, Focacci F, Stipo G. Structural behavior of arch models strengthened using fiber-reinforced polymer strips of different lengths. J Compos Constr 2013;17(2):249–58. https://doi.org/10.1061/(ASCE)CC.1943-5614.0000325.

[26] Briccoli Bati S, Rovero L, Tonietti U. Strengthening masonry arches with composite materials. J Compos Constr 2007;11(1):33–41. https://doi.org/10.1061/(ASCE)1090-0268(2007)11:1(33).

[27] Borri A, Castori G, Corradi M. Intrados strengthening of brick masonry arches with composite materials. ISSN 1359-8368 Compos Part B: Eng 2011;42(5):1164–72. https://doi.org/10.1016/j.compositesb.2011.03.005.

[28] Alecci V, Misseri G, Rovero L, Stipo G, De Stefano M, Feo L, Luciano R. Experimental investigation on masonry arches strengthened with PBO-FRCM composite. ISSN 1359-8368 Compos Part B: Eng 2016;100:228–39. https://doi.org/10.1016/j.compositesb.2016.05.063.

[29] Malena M, de Felice G. Debonding of composites on a curved masonry substrate: Experimental results and analytical formulation. Compos Struct 2014;112:194–206. https://doi.org/10.1016/j.compstruct. 2014.02.004.

[30] Malena M. Closed-form solution to the debonding of mortar based composites on curved substrates. " Compos, Part B 2018;139:249–58. https://doi.org/10.1016/j.compositesb.2017.11.044.

[31] De Santis S. Bond behaviour of steel reinforced grout for the extrados strengthening of masonry vaults. Constr Build Mater 2017;150:367–82. https://doi.org/10.1016/j.conbuildmat.2017.06.010.

[32] Bertolesi E, Grande E, Fagone M, Milani G, Rotunno T. Mechanical model based on a BVP for FRPs applied on flat and curved masonry pillars with anchor spikes. Compos Struct 2021;273:114251. https://doi.org/10.1016/j.compstruct.2021.114251.

[33] Bertolesi E, Milani G, Fagone M, Rotunno T, Grande E. Heterogeneous FE model for single lap shear tests on FRP reinforced masonry curved pillars with spike anchors. Constr Build Mater 2020;258:119629. https://doi.org/10.1016/j.conbuildmat.2020.119629.

[34] Rotunno T, Fagone M, Bertolesi E, Grande E, Milani G. Single lap shear tests of masonry curved pillars externally strengthened by CFRP strips. Compos Struct 2018;200:434–48. ⟨https://doi.org/10.1016/j.compstruct.2018.05.097⟩.

[35] Rotunno T, Fagone M, Bertolesi E, Grande E, Milani G. Curved masonry pillars reinforced with anchored CFRP sheets: An experimental analysis. Compos, Part B 2019;174:107008. https://doi.org/10.1016/j.compositesb.2019.107008.

[36] Zampieri P, Santinon D, Pellegrino C, Iodice F, Vecchi A. Effect of Spike Anchors in the Bond Behavior of FRCM Systems Applied onto Curved Masonry Substrates (art. no) J Compos Constr 2023;27(6):04023061. https://doi.org/10.1061/JCCOF2.CCENG-4199.

[37] Liu B, Kawabe D, Kim C, Sarhosis V. Full life-cycle vibration-based monitoring of a full-scale masonry arch bridge with increasing levels of damage. Eng Struct 2024;315. https://doi.org/10.1016/j.engstruct.2024.118466.

[38] Sarhosis V, Liu B, Gilbert M. The 3d response of a large-scale masonry arch bridge - part I: Performance under low and medium loading levels. Eng Struct 2024;316. https://doi.org/10.1016/j.engstruct.2024.118496.

[39] Boem I, Gattesco N. Cyclic behavior of masonry barrel vaults strengthened through Composite Reinforced Mortar, considering the role of the connection with the abutments. ISSN 0141-0296 Eng Struct 2021;228:111518. https://doi.org/10.1016/j.engstruct.2020.111518.

[40] Barducci S, Alecci V, De Stefano M, Misseri G, Rovero L, Stipo G. Experimental and Analytical Investigations on Bond Behavior of Basalt-FRCM Systems (art. no) J Compos Constr 2020;24(1):04019055. https://doi.org/10.1061/(ASCE)CC.1943-5614.0000985.

[41] Carozzi FG, Poggi C, Bertolesi E, Milani G. Ancient masonry arches and vaults strengthened with TRM, SRG and FRP composites: Experimental evaluation. ISSN 0263-8223 Compos Struct 2018;187:466–80. https://doi.org/10.1016/j.compstruct.2017.12.075.

[42] De Santis S, de Felice G, Roscini F. Retrofitting of masonry vaults by basalt textile-reinforced mortar overlays. Int, J Archit Herit 2019;13(7):1061–77. https://doi.org/10.1080/15583058.2019.1597947.

[43] Gattesco N, Boem I, Andretta V. Experimental behaviour of non-structural masonry vaults reinforced through fiber-reinforced mortar coating and subjected to cyclic horizontal loads. ISSN 0141-0296 Eng Struct 2018;172:419–31. https://doi.org/10.1016/j.engstruct.2018.06.044.

[44] Gioffré M, Navarra G, Cavalagli N, Lo Iacono F, Gusella V, Pepi C. Effect of hemp bio composite strengthening on masonry barrel vaults damage. ISSN 0950-0618 Constr Build Mater 2023;367:130100. https://doi.org/10.1016/j.conbuildmat.2022.130100.

[45] Kariou FA, Triantafyllou SP, Bournas DA. TRM strengthening of masonry arches: An experimental investigation on the effect of strengthening layout and textile fiber material. ISSN 1359-8368 Compos Part B: Eng 2019;173:106765. https://doi.org/10.1016/j.compositesb.2019.04.026.

[46] Sadeghi NH, Oliveira DV, Silva RA, Mendes N, Correia M, Azizi-Bondarabadi H. Experimental characterization of adobe vaults strengthened with a TRM-based compatible composite. ISSN 0950-0618 Constr Build Mater 2021;271:121568. https://doi.org/10.1016/j.conbuildmat.2020.121568.

[47] Augusthus-Nelson L, Swift G. Experimental investigation of the residual behaviour of damaged masonry arch structures. ISSN 2352-0124 Structures 2020;27:2500–12. https://doi.org/10.1016/j.istruc.2020.08.008.

[48] Augusthus-Nelson L, Swift G, Melbourne C, Smith C, Gilbert M. Large-scale physical modelling of soil-filled masonry arch bridges. Int J Phys Model Geotech 2017;18:1–14. https://doi.org/10.1680/jphmg.16.00037.

[49] Bednarz L., Górski A., Jasieńko J., Rusiński E. Simulations and analyses of arched brick structures. Autom Constr 2011;20(7):741–54. ⟨https://doi.org/10.1016/j.autcon.2011.01.005.

[50] Misseri G, Rovero L, Stipo G, Barducci S, Alecci V, De Stefano M. Experimental and analytical investigations on sustainable and innovative strengthening systems for masonry arches. ISSN 0263-8223 Compos Struct 2019;210:526–37. https://doi.org/10.1016/j.compstruct.2018.11.054.

[51] Garmendia L, Larrinaga P, San-Mateos R, San-José J T. Strengthening masonry vaults with organic and inorganic composites: An experimental approach. ISSN 0264-1275 Mater Des 2015;85:102–14. https://doi.org/10.1016/j.matdes.2015.06.150.

[52] Alejo LE, Mendes N, Lourenço PB, Martínez G. Protecting the historic buildings of Mexico: The barrel Vault of San Agustin Church in Morelia. J Perform Constr Facil 2021;35. https://doi.org/10.1061/(ASCE)CF.1943-5509.0001556 (doi).

[53] Tedesco A, Forestieri G. FRCM reinforcement systems in historical masonries of Savuto Castle, Italy. J Archit Eng 2019;25:05019003. https://doi.org/10.1061/(ASCE)AE.1943-5568.0000347 (doi).

[54] Demir C, Comert M, Inci P, Dusak S, Ilki A. Seismic retrofitting of the 19th century hirka-i serif mosque using textile reinforced mortar. Int J Archit Herit 2022. https://doi.org/10.1080/15583058.2022.2038305.

[55] Zampieri P, Simoncello N, Gonzalez-Libreros J, Pellegrino C. Evaluation of the vertical load capacity of masonry arch bridges strengthened with FRCM or SFRM by limit analysis (art. no) Eng Struct 2020;225:111135. https://doi.org/10.1016/j.engstruct.2020.111135.

[56] Zampieri P. Horizontal capacity of single-span masonry bridges with intrados FRCM strengthening (art. no) Compos Struct 2020;244:112238. https://doi.org/10.1016/j.compstruct.2020.112238.

[57] D'Ambrisi A, Focacci F, Luciano R, Alecci V, De Stefano M. Carbon-FRCM materials for structural upgrade of masonry arch road bridges. ISSN 1359-8368 Compos Part B: Eng 2015;75:355–66. https://doi.org/10.1016/j.compositesb.2015.01.024.

[58] D'Ambrisi A, Focacci F, Caporale A. Strengthening of masonry–unreinforced concrete railway bridges with PBO-FRCM materials. ISSN 0263-8223 Compos Struct 2013;102:193–204. https://doi.org/10.1016/j.compstruct.2013.03.002.

[59] Michele Paradiso, Stefano Galassi, Daniela Sinicropi (2014). "Stabilità di archi e volte in muratura: metodi tradizionali e calcolo automatico", in "Patologia della Costruccion, Tecnologia de la Rehabilitacion y Gestion del Patrimonio", Luis Villegas, Ignacio Lombillo, Clara Liano, Haydee Blanco (Eds.), Gráficas Iguña, S.A., Proc. of Latin American Congress on "Construction Pathology, Rehabilitation Technology and Heritage Management (Rehabend 2014), Santander, Spain, 1–4 April 2014, pp. 960–969, ISSN 2386–8198, ISBN: 978–84-606–6738-4.

[60] Bertolesi E, Milani G, Carozzi FG, Poggi C. Ancient masonry arches and vaults strengthened with TRM, SRG and FRP composites: numerical analyses. ISSN 0263-8223 Compos Struct 2018;187:385–402. https://doi.org/10.1016/j.compstruct.2017.12.021.

[61] Bertolesi E, Grande E, Fagone M, Milani G, Rotunno T. Mechanical model based on a BVP for FRPs applied on flat and curved masonry pillars with anchor spikes. ISSN 0263-8223 Compos Struct 2021;273:114251. https://doi.org/10.1016/j.compstruct.2021.114251.

[62] Castellano A, Fraddosio A, Oliveira DV, Piccioni MD, Ricci E, Sacco E. An effective numerical modelling strategy for FRCM strengthened curved masonry structures. ISSN 0141-0296 Eng Struct 2023;274:115116. https://doi.org/10.1016/j.engstruct.2022.115116.

[63] Scacco J, Milani G, Lourenço PB. A micro-modeling approach for the prediction of TRM bond performance on curved masonry substrates. ISSN 0263-8223 Compos Struct 2021;256:113065. https://doi.org/10.1016/j.compstruct.2020.113065.

[64] Grande E, Milani G. Modeling of FRCM strengthening systems externally applied on curved masonry substrates. ISSN 0141-0296 Eng Struct 2021;233:111895. https://doi.org/10.1016/j.engstruct.2021.111895.

[65] Alecci Valerio, Galassi Stefano, Mistretta Fausto, Stipo Gianfranco, De Stefano Mario. Stability assessment of masonry arches reinforced with fiber-reinforced composite materials under large deformation. In: Gabriele S, Manuello Bertetto A, Marmo F, Micheletti A, editors. Shell and Spatial Structures. IWSS 2023. Lecture Notes in Civil Engineering, 437. Cham: Springer; 2024. p. 737–46. https://doi.org/10.1007/978-3-031-44328-2_77.

[66] Stefano Galassi (2018). "Analysis of masonry arches reinforced with FRP sheets: experimental results and numerical evaluations", MATEC Web of Conferences, 207, 01002, ⟨https://doi.org/10.1051/matecconf/201820701002⟩, Proc. of International Conference on Metal Material Processes and Manufacturing (ICMMPM2018) (19–20 July 2018, Jeju Island, South Korea).

[67] Stefano Galassi. A numerical procedure for failure mode detection of masonry arches reinforced with fiber reinforced polymeric materials. IOP Conf Ser: Mater Sci Eng 2018;369(1):012038. https://doi.org/10.1088/1757-899X/369/1/

012038. Proc. of 5th Global Conference on Polymer and Composite Materials (PCM 2018) (10-13 April 2018, Kitakyushu City, Japan).
[68] Zampieri P. Horizontal capacity of single-span masonry bridges with intrados FRCM strengthening. Compos Struct 2020;244. https://doi.org/10.1016/j.compstruct.2020.112238.
[69] Drosopoulos GA, Stavroulakis GE, Massalas CV. FRP reinforcement of stone arch bridges: unilateral contact models and limit analysis. Compos Part B: Eng 2007;38 (2):144–51. https://doi.org/10.1016/j.compositesb.2006.08.004.